

# Mechanics of evenly spaced strike-slip faults and its implications for the formation of tiger-stripe fractures on Saturn's moon Enceladus



An Yin<sup>a,\*</sup>, Andrew V. Zuza<sup>a</sup>, Robert T. Pappalardo<sup>b</sup>

<sup>a</sup>Department of Earth, Planetary, and Space Sciences and the Institute of Planets and Exoplanets, University of California, Los Angeles, CA 90095-1567, USA

<sup>b</sup>M/S 321-560, Jet Propulsion Laboratory, California Institute of Technology, Pasadena, CA 91109, USA

## ARTICLE INFO

### Article history:

Received 10 July 2015

Revised 16 October 2015

Accepted 29 October 2015

Available online 11 November 2015

### Keyword:

Enceladus

Ices

Mechanical properties

Tectonics

## ABSTRACT

We present the first mechanical analysis based on realistic rheology and boundary conditions on the formation of evenly spaced strike-slip faults. Two quantitative models employing the stress-shadow concept, widely used for explaining extensional-joint spacing, are proposed in this study: (1) an empirically based stress-rise-function model that simulates the brittle-deformation process during the formation of evenly spaced parallel strike-slip faults, and (2) an elastic plate model that relates fault spacing to the thickness of the fault-hosting elastic medium. When applying the models for the initiation and development of the tiger-stripe fractures (TSF) in the South Polar Terrain (SPT) of Enceladus, the mutually consistent solutions of the two models, as constrained by the mean spacing of the TSF at  $\sim 35$  km, requires that the brittle ice-shell thickness be  $\sim 30$  km, the elastic thickness be  $\sim 0.7$  km, and the cohesive strength of the SPT ice shell be  $\sim 30$  kPa. However, if the brittle and elastic models are decoupled and if the ice-shell cohesive strength is on the order of  $\sim 1$  MPa, the brittle ice shell would be on the order of  $\sim 10$  km.

© 2015 Elsevier Inc. All rights reserved.

## 1. Introduction

Researchers generally agree that the geologically active South Polar Terrain (SPT) of Saturn's icy moon Enceladus lies over a regional sea (Collins and Goodman, 2007; Iess et al., 2014; McKinnon, 2015), or even a global ocean (Patthoff and Kattenhorn, 2011; McKinnon, 2015; Thomas et al., 2015), with a total ice shell thickness of 30–40 km above a liquid water layer (Iess et al., 2014). However, they strongly disagree on the thickness of its brittle ice shell, with current estimates varying from 2 km to 35 km (Gioia et al., 2007; Smith-Konter and Pappalardo, 2008). The large discrepancy can be attributed to the fact that different studies assume different physical processes for the formation of the tiger-stripe fractures (TSF), the most dominant tectonic features within the SPT (Porco et al., 2006) (Fig. 1). Based on modeling shear heating along the TSF, Roberts and Nimmo (2008) derive a minimum value of  $\sim 5$  km for the SPT ice-shell thickness. By quantifying the effect of tidal stress on driving alternating strike-slip motion along the TSF, Smith-Konter and Pappalardo (2008) and Olgin et al. (2011) show that the SPT ice shell is thicker than 2–4 km but must be thinner than  $\sim 40$  km. Rudolph and Manga (2009) treat the TSF as propagating tensile cracks and in this physical context they find

that the SPT ice shell is likely to be thinner than  $\sim 25$  km. Assuming that (1) the TSF have an extensional origin and (2) the fracture-hosting ice-shell thickness equals to the spacing of the TSF, Gioia et al. (2007) inferred the thickness of the SPT ice shell to be  $\sim 35$  km without providing a quantitative mechanical reason. Helfenstein and Porco (2015) suggest that the brittle ice shell near the tiger-stripe fractures is  $\sim 5$  km assuming that the spacing of their observed minor en echelon shear fractures within the TSF zones has a 1:1 ratio to the ice shell thickness. Similar to the work of Gioia et al. (2007), Helfenstein and Porco (2015) did not provide the mechanical basis for the assumed spacing vs. layer thickness ratio.

Except the work of Helfenstein and Porco (2015), most of the aforementioned ice-shell thickness estimates are based on the view that the TSF were initiated as tensile fractures and were later reactivated as strike-slip faults with alternating senses of shear driven by the diurnal tidal stress (Gioia et al., 2007; Nimmo et al., 2007; Matsuyama and Nimmo, 2008; Helfenstein et al., 2006, 2008; Rudolph and Manga, 2009; Patthoff and Kattenhorn, 2011; Walker et al., 2012). However, this widely accepted scenario is challenged by new geologic mapping based on a systematic and detailed structural investigation of major fracture zones in the SPT using high-resolution images (Yin and Pappalardo, 2015). Specifically, the kinematic analysis shows that the TSF were initiated and have continued to move as left-slip faults (Yin and

\* Corresponding author.

E-mail addresses: [yin@ess.ucla.edu](mailto:yin@ess.ucla.edu), [ayin54@gmail.com](mailto:ayin54@gmail.com) (A. Yin), [Robert.Pappalardo@jpl.nasa.gov](mailto:Robert.Pappalardo@jpl.nasa.gov) (R.T. Pappalardo).

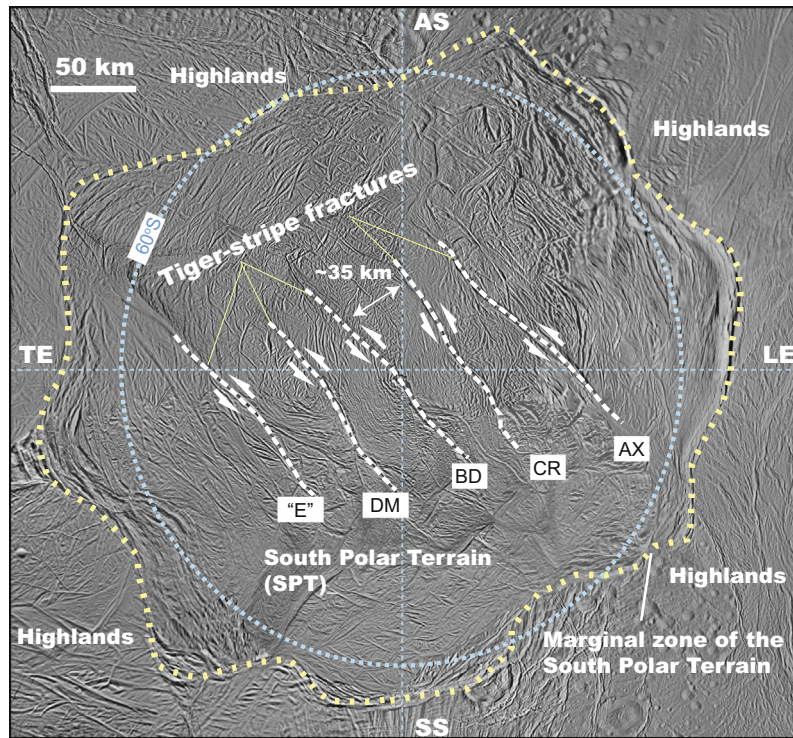


**Fig. 1.** Simplified tectonic map of the South Polar Terrain based on the analysis of images obtained by Cassini orbiter's Imaging Science Subsystem (ISS) and constructed by the CICLOPS team (i.e., Cassini imaging team); the mosaic is in the south polar projection. Tiger-stripe fractures in the South Polar Terrain of Saturn's moon Enceladus. Each fracture is  $\sim 135$  km long and spaced  $\sim 35$  km from one another. The left-slip fault interpretation is based on the work of Yin and Pappalardo (2015). Coordinate points SS, AS, LE, and TE are longitudinal directions from the South Pole pointing toward the sub-saturnian ( $0^\circ$  longitude), anti-saturnian ( $180^\circ$ W), leading-edge ( $90^\circ$ W), and trailing-edge ( $270^\circ$ W) points on the equator of Enceladus, respectively. Abbreviations: AX, Alexandria fracture; CR, Cairo fracture; BD, Baghdad fracture; DM, Damascus fracture; "E", a newly designated fracture by Yin and Pappalardo (2015).

Pappalardo, 2015) (Fig. 1) with perturbations as transient tensile fractures induced by tidal stress (Nimmo et al., 2014). The revelation that the TSF are left-slip structures (Yin and Pappalardo, 2015) demands a new mechanical scheme that is capable of relating the well documented TSF spacing ( $\sim 35$  km) (Fig. 1) to the SPT ice-shell thickness and the mechanical properties of the TSF and hosting icy crust on Enceladus.

When searching through the existing literature, we were surprised to find that a physical model, *with realistic boundary conditions and elastic rheology* (cf., Roy and Royden, 2000a, 2000b) for brittle crust deformation, that relates the spacing of strike-slip faults to the thickness of the brittle layer hosting the faults has never been developed, although parallel and evenly spaced strike-slip faults occur widely on Earth. Terrestrial examples of parallel strike-slip fault systems include those spaced at  $\sim 40$  km along the southern San Andreas system (e.g., Sylvester, 1988), at 300–400 km across central Asia (e.g., Yin, 2010), at 200–300 km in central and northern Tibet (Yin and Harrison, 2000; Taylor et al., 2003; Taylor and Yin, 2009), and (4) at 150–400 km in northern China (e.g., Yin et al., 2015). In this study, we address the fundamental question of *what controls the spacing of parallel strike-slip faults* by developing a new quantitative model based on the stress-shadow concept of Lachenbruch (1961).

The stress-shadow concept states that the formation of an extensional fracture in a layer of rock under regional extension imposes a local stress-boundary condition that causes stress-magnitude reduction next to the fracture. This process is commonly referred to as the *stress-shadow effect* (Lachenbruch, 1961), which creates regions of low stress magnitude below the tensile strength of intact rock next to the fracture. Because of this effect, no new fractures can be generated within the low-stress regions immediately next to the early formed fractures; the critical dis-

tance defining the width of the low-stress zone measures the length of stress shadow. As new extensional fractures can only be created immediately outside the stress shadow, and the stress shadow length must be equal to the fracture spacing. It is this simple concept that has been used to quantify the occurrence of evenly spaced extensional joints on Earth (e.g., Pollard and Segall, 1987; Gross, 1993).

In this study, we use the stress-shadow concept of Lachenbruch (1961) to formulate three quantitative models for the formation of parallel strike-slip faults. The first model is based on an analytical solution of stress distribution induced by movement on an anti-plane (i.e., mode-III) crack driven by a remote fault-parallel shear stress (i.e., strike-slip motion on a crack). As detailed below, this model, based on linear elastic fracture mechanics, is appropriate for modeling shallow faults within the uppermost part of the Earth's crust, but it is unrealistic for modeling the TSF that cut through the entire SPT ice shell (Porco et al., 2006). To overcome this limitation, we derive two alternative models by assuming that the SPT ice shell deforms either as a perfect plastic material governed by the Coulomb fracture criterion (also known as Coulomb failure criterion) or as a linear elastic solid governed by Hooke's law. Using these two models, we estimate the brittle ice-shell thickness to be  $\sim 30$  km, the elastic thickness to be  $\sim 0.7$  km, and the cohesive strength of the ice shell to be  $\sim 30$  kPa for the South Polar Terrain that hosts the tiger-stripe fractures.

## 2. Stress-strain curves for ice deformation in the elastic and plastic regimes

It has been long known that the stress-strain relationships for ice are similar to those of rocks (e.g., Sinha, 1978; Hutter, 1983;

Schulson, 2001). That is, under a low-stress condition the induced strain is elastic and linearly proportional to stress as described by Hooke's law (e.g., Sinha, 1978) (Fig. 2A). When stress is higher than the elastic limit, the corresponding strain is non-linearly related to the stress and the induced deformation is irreversible (i.e., plastic) (Sinha, 1978; Hutter, 1983; Mellor and Cole, 1983) (Fig. 2A). A continuous increase in the stress magnitude leads to brittle failure as expressed by the formation of fractures (Schulson, 2001) (Fig. 2A).

As the shear-stress magnitude increases with depth in an ice shell (Fig. 2A), we envision that the topmost part of the SPT ice shell behaves elastically (Fig. 2B). That is, deformation in this portion of the ice shell is reversible once the load is removed. In reality, the top elastic layer of the ice shell may behave visco-elastically and its rheological behavior is determined by the Maxwell time, defined as  $\tau = \frac{\eta}{E}$ , where  $E$  is the elastic shear modulus and  $\eta$  is the Newtonian viscosity of the ice shell, respectively (see Table 1 for definition of all variables used in this study). Deformation of the ice shell is dominantly elastic for  $\tau \ll 1$  but viscous for  $\tau \gg 1$ . In this study, we neglect viscous deformation and focus only on the mechanical controls for the initiation of the TSF and the

subsequent maintenance of their motion via elastic and brittle deformation.

At a greater depth where shear stress magnitude is high, the stress magnitude exceeds the elastic limit and deformation of the ice shell behaves plastically (Fig. 2B). For both plastic and elastic deformation, we envision that their brittle failure is controlled by the same Coulomb fracture criterion, which is expressed as the brittle fracture strength envelope in Fig. 2B. In the models development below, we assume that the SPT ice shell is either entirely elastic as shown in Fig. 2C, or completely plastic as shown in Fig. 2D. This treatment allows us to estimate the elastic and plastic thickness of the SPT ice shell as end-member cases, labeled as  $h_E$  and  $h_B$  in Fig. 2C and D, respectively.

### 3. A stress-shadow model based on a fracture mechanics solution

The basic idea of a stress-shadow model may be illustrated by a sequential formation of extensional fractures (Lachenbruch, 1961; Nur, 1982; Pollard and Segall, 1987) (Fig. 3A–C). A layer of rock is under regional extension induced by exerting a remote normal

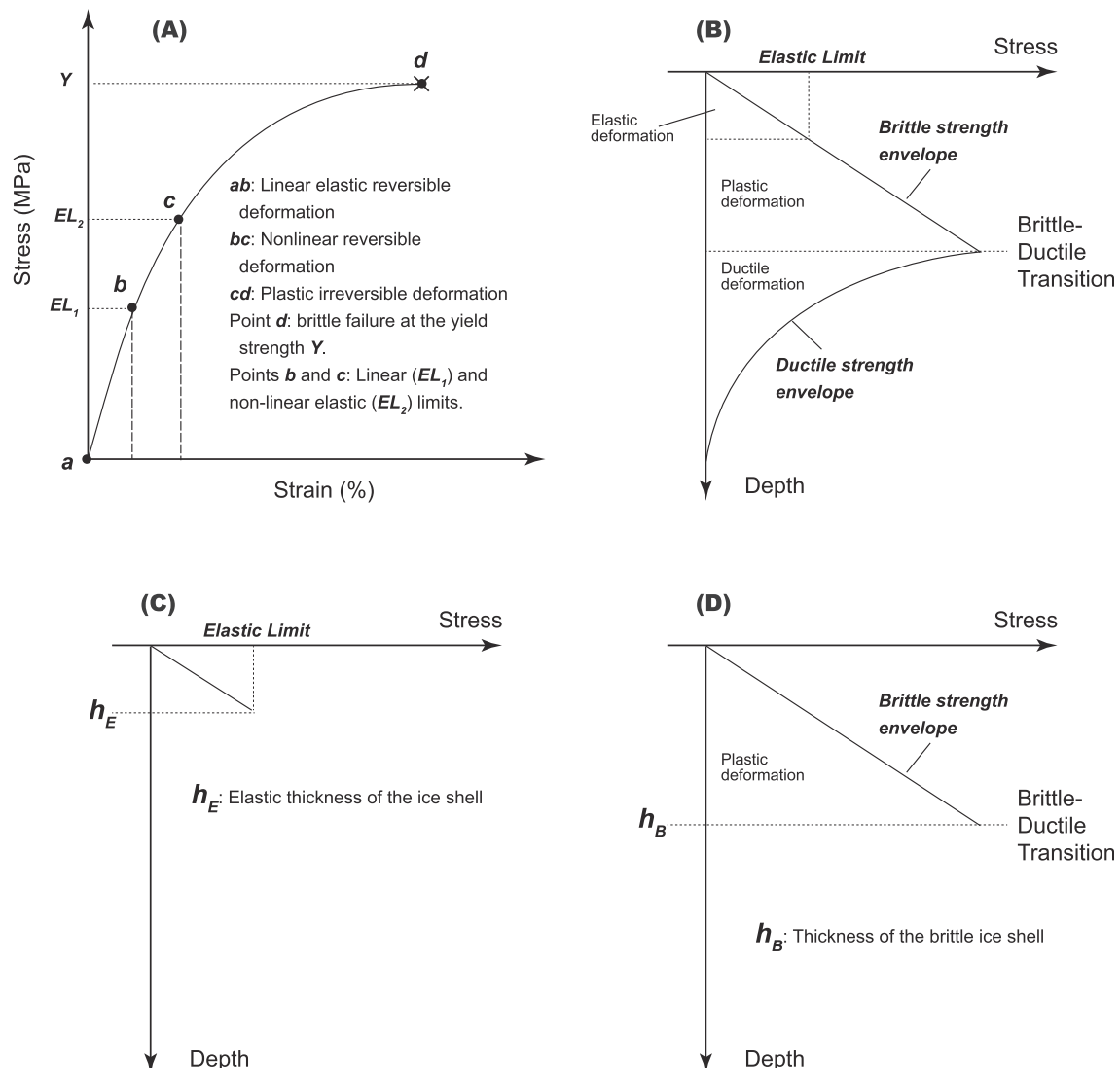


**Fig. 2.** (A) A typical stress–strain curve for ice under uniaxial deformation (see text for details). (B) Proposed depth-dependent rheological profile of the SPT ice shell. (C) End-member model assuming the brittle ice shell of the SPT is composed of only an elastic layer. (D) End-member model assuming that the brittle ice shell of the SPT is composed of only a plastic layer.

**Table 1**

Model parameters and references. Sources: [Ref. 1]: These values were converted from the experimentally determined uniaxial tensile strength of fresh-water and salt-water ice at  $-10\text{ }^{\circ}\text{C}$  and  $-40\text{ }^{\circ}\text{C}$  reported in Schulson (2001). [Refs. 2 and 3]: Dempsey et al. (1999) and Dempsey (2000). [Ref. 4]: Schulson (2002). [Ref. 5]: Schulson and Fortt (2012). [Ref. 6]: We use the density of sea ice from Timco and Frederking (1996) for the South Polar Terrain (SPT) ice shell. This is because the SPT surface is very young and nearly free of craters, raising the possibility that the entire ice shell was juvenile rather than reworked. [Ref. 7]: According to less et al. (2014), the density of the warm ice in the SPT is  $\sim 8\%$  higher than that of the cold brittle ice above. [Ref. 8]: Schenk and McKinnon (2009). [Ref. 9]: Porco et al. (2006). SPT = South Polar Terrain.

Physical parameters	Symbol	Value used in model calculations
Elastic shear modulus	$E$	Not used in model calculation
Newtonian viscosity	$\eta$	Not used in model calculation
The Maxwell time	$\tau = \eta/E$	$\tau \ll 1$
Normal stress	$\sigma_n$	
Shear stress	$\sigma_s$	
Regional normal stress during formation of tensile cracks	$\sigma_n^r$	
Normal stress on an extensional fracture surface	$\sigma_n^c$	
Tensile strength of rock/ice	$T$	
Shear stress on a strike-slip fault	$\sigma_s^c$	
Shear strength of the SPT ice shell	$Y$	
Shear strength of the ice shell bounding the SPT	$Y^{BR}$	
Depth-averaged shear strength in and outside the SPT	$\bar{Y}, \bar{Y}^{BR}$	Determined from shear strength of ice
Elastic and brittle ice-shell thickness of the SPT	$h_E, h_B$	Determined by models from this study
Ice-shell thickness in regions outside the SPT	$H$	Determined using Airy isostasy
Frictional cohesive strength of the tiger-stripe fractures	$C_1$	Set to be zero in this study
Cohesive strength of intact ice within and outside the SPT	$C_0 = C_{BR}$	$1.7\text{--}5.7$ [Ref. 1] or $11\text{--}38\text{ kPa}$ [Refs. 2,3]
Pore-fluid pressure ratios in ice and along fault surface	$\lambda_\phi, \lambda_f$	Set to be zero
Coefficient of internal friction/friction of ice and fault	$\mu_\phi$ and $\mu_f$	Same as the effective coefficients
Effective internal coefficient of friction of intact ice	$\bar{\mu}_\phi = \bar{\mu}_\phi^{BR}$	$0.53\text{--}0.58$ [Ref. 4]
Effective coefficient of friction for the tiger-stripe fractures	$\bar{\mu}_f$	$0.37\text{--}0.53$ [Ref. 5]
Acceleration of surface gravity on Enceladus	$g$	$0.133\text{ m/s}^2$
Density of the cold brittle ice shell	$\rho_1$	$720\text{--}940\text{ kg/m}^3$ [Ref. 6]
Density of the warm ductile ice shell	$\rho_2$	$990\text{ kg/m}^3$ [Ref. 7]
Topographic relief between the SPT and surrounding area	$e$	$0.5\text{--}1.0\text{ km}$ [Ref. 8]
Brittle ice-shell thickness of the SPT	$h$	Estimated in this study
Spacing of tiger-stripe fractures	$S$	$35\text{ km}$ [Ref. 9]

stress ( $\sigma_n$ ) that has a magnitude of  $\sigma_n = \sigma_n^r$  (Fig. 3A). If the magnitude of the remote stress  $\sigma_n^r$  is higher than the tensile strength of the rock,  $T$ , fractures in the rock layer will be created (Fig. 3B).

Once formed, the presence of the newly created extensional fracture enforces a local stress-boundary condition (Fig. 3B). In modeling extensional joints, the normal stress on the fracture surface ( $\sigma_n^c$ ) is commonly set to be zero (i.e., it is treated as a stress-free surface; see Pollard and Segall, 1987). This stress-free condition on the extensional-fracture surface causes reduction of the normal-stress magnitude in regions immediately next to the fracture (Fig. 3B). The stress reduction in turn introduces the *stress shadow effect*, which is expressed by the existence of regions next to a fracture that has normal-stress magnitude below the tensile strength of intact rock (Fig. 3B).

Because of the stress-shadow effect, other extensional fractures, which were created either simultaneously or at later times than the fracture mentioned above and shown in Fig. 3B, can only form

immediately outside the stress shadow regions (Fig. 3C). The averaged spacing of the fractures should be equal to the length of the stress shadow,  $S$ , although the spacing may vary from  $S$  to  $<2S$  as no new fractures can be created within the overlapping stress shadows of the two neighboring fractures. The length of the stress shadow, equals to the fractures spacing ( $S$ ), can be defined by the following relationship:

$$\sigma_n(x = S) = T \quad (1)$$

where  $T$  is the tensile strength of the crack-hosting medium and  $\sigma_n(x)$  is the normal stress within the rock layer as a function of distance from the fracture (Fig. 3B). We use the sign convention of positive for tensile stress in this study.

If the tensile strength  $T$  is uniform in the medium under extension, the resulting extensional joint spacing should be a constant. The joint spacing,  $S$ , can be determined by solving Eq. (1) if the functional form of  $\sigma_n(x)$  is known. In existing studies, the relationship between joint spacing and the tensile strength of the joint-hosting medium is determined by a linear-elastic-fracture-mechanics (LEFM) solution of stress distribution induced by the presence of a mode-I crack in an infinite elastic medium under regional extension (Lachenbruch, 1961; Pollard and Segall, 1987). That is, an extensional joint is approximated as an opening (i.e., mode-I) crack.

Because strike-slip faults are commonly treated as anti-plane (i.e., mode-III) cracks, a similar approach may be adopted by determining the relationship between strike-slip-fault spacing and the shear strength of the fault-bounded domains consisting of intact rock/ice under regional strike-slip shear. A key difference between an extensional crack and a strike-slip anti-plane crack is that the magnitude of the shear stress on an anti-plane crack is not zero, but instead equals to the frictional strength of the crack plane (cf., Roy and Royden, 2000a, 2000b). As long as the regional stress is greater in magnitude than both the fault frictional strength and the shear fracture strength of the intact fault-hosting rock/ice, the stress-shadow mechanism should operate and evenly spaced strike-slip faults should form if all the strike-slip faults have the same frictional strength and the fault hosting layer has the same shear-fracture strength (Fig. 3E; cf. Fig. 3D). In contrast, spatial variability of fault strength and/or the shear-fracture strength of the fault-bounded ice and crustal domains would lead to the formation of unevenly spaced parallel strike-slip faults (Fig. 3D).

Treating the strike-slip faults as mode-III cracks in an elastic half space, the shear stress parallel to the direction of strike-slip motion can be written as (Pollard and Segall, 1987):

$$\sigma_{xz}(r) = \sigma_s^r + (\sigma_s^r - \sigma_s^c)[rR^{-1} \cos(\theta - \Theta) - 1] \quad (2)$$

where  $r$  and  $\theta$  are the coordinate variables in a polar coordinate system,  $R = \sqrt{r_1^2 + r_2^2}$ ,  $\Theta = (\theta_1 + \theta_2)/2$  (Fig. 4A),  $\sigma_{xz}(r)$  is the shear stress in the fault-motion direction,  $\sigma_s^r$  is the regional shear stress parallel to the crack assumed to be constant with depth, and  $\sigma_s^c$  is the shear stress on the fault plane also assumed to be constant over the fault plane. The Cartesian coordinate axes  $x_1 = x$ ,  $x_2 = y$ , and  $x_3 = z$  are defined in Fig. 4B. Note that  $x_1 = x$  and  $x_3 = z$  lie on the surface following the convention in fracture mechanics, with  $x_1 = x$  perpendicular to the fault. The shear stress in the fault-slip direction at the surface can be evaluated using Eq. (2) (Pollard and Segall, 1987) as:

$$\sigma_{xz}(x) = \sigma_s^r + (\sigma_s^r - \sigma_s^c) \left[ \frac{|x|}{(x^2 + h^2)^{1/2}} - 1 \right] \quad (3)$$

where  $x$  is the distance from the vertical fault at the surface, and  $h$  is the fault depth in the  $y$  direction (Fig. 4). If the surface shear stress in Eq. (2) creates new strike-slip faults next to an earlier formed fault and the shear-fracture strength of the fault-bounded domains

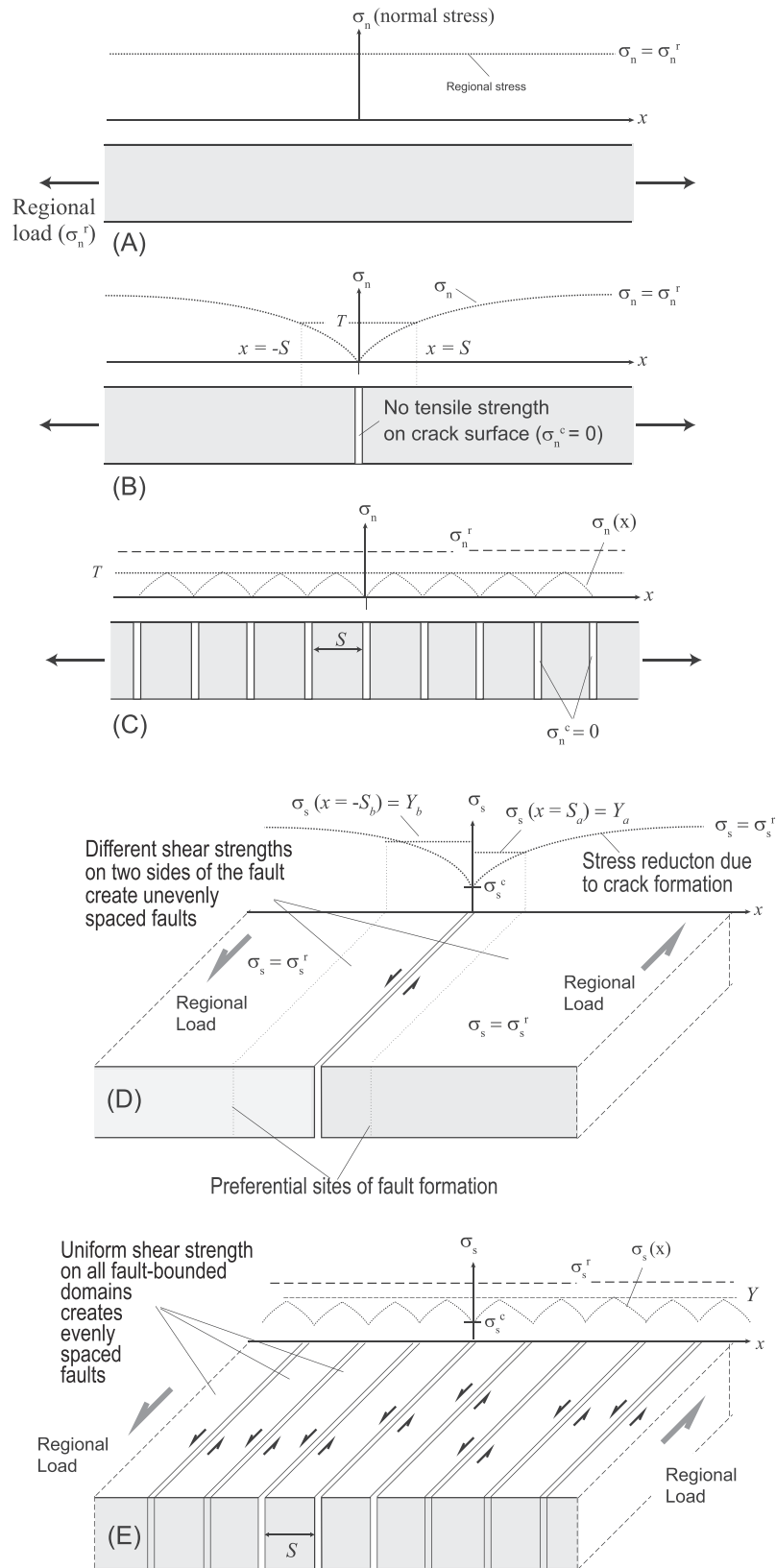


**Fig. 3.** (A)–(C), a conceptual model for the formation of evenly spaced joints due to the stress-shadow effect. (A) A layer is under regional extension with a remote normal stress  $\sigma_n = \sigma_n^r$ . (B) The presence of a fracture would cause local stress reduction and this shadow effect would prevent fractures to form within a critical distance  $S$ . (C) Because of the stress-shadow effect, the formation of the fractures in the deformed region are spaced by the critical distance  $S$ . (D) and (E) Explanation for the formation of the evenly spaced strike-slip faults due to the stress-shadow effect. See text for details.

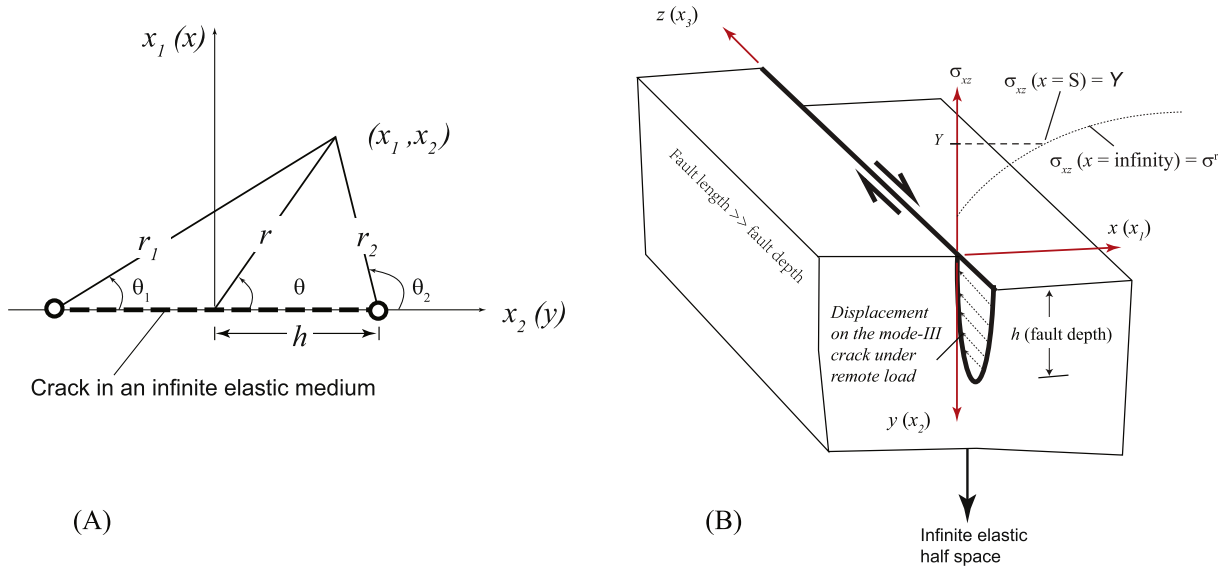


**Fig. 4.** (A) Relationship between polar and Cartesian coordinate systems for solving an anti-crack problem using linear elastic fracture mechanics. See text for the definition of the symbols in the sketch. (B) A strike-slip fault is treated as an anti-plane crack in an elastic half space. The off-fault shear stress  $\sigma_{xz}$  satisfies the boundary conditions of  $\sigma_{xz}(x=0) = \sigma_s^c$  and  $\sigma_{xz}(x=\infty) = \sigma_s^r$ .

is uniform, then the stress-shadow length ( $S$ ) that equals to the fault spacing can be defined by:

$$\sigma_{xz}(x=S) = Y = \sigma_s^r + (\sigma_s^r - \sigma_s^c) \left[ \frac{S}{(S^2 + h^2)^{1/2}} - 1 \right] \quad (4)$$

where  $Y$  is the shear-fracture strength of the fault-bounded domains and  $\sigma_s^c$  is the shear stress on the fault. The regional stress and the stress on the fault plane are constrained by the rock shear-fracture strength and the fault frictional strength, which can be obtained respectively by their vertically averaged values as

$$\bar{\sigma}_s^c = \frac{1}{h} \int_0^h (C_1 + \bar{\mu}_f \rho_1 g y) dy = C_1 + \frac{1}{2} \bar{\mu}_f \rho_1 g h \quad (5)$$

and

$$\bar{Y} = \frac{1}{h} \int_0^h (C_0 + \bar{\mu}_\phi \rho_1 g y) dy = C_0 + \frac{1}{2} \bar{\mu}_\phi \rho_1 g h \quad (6)$$

where  $\bar{\sigma}_s^c$  is the vertically averaged frictional strength on the fault plane, and  $\bar{Y}$  is the vertically averaged rock shear-fracture strength,  $h$  is the fault depth in the elastic half space,  $\rho_1$  is the density of the fault-bounded medium,  $g$  is the gravitational acceleration,  $y$  is a coordinate axis pointing downward,  $C_0$  and  $\bar{\mu}_\phi$  are the cohesive strength and the effective coefficient of *internal friction* for the fault-bounded domains, and  $C_1$  and  $\bar{\mu}_f$  are the cohesive strength and the effective coefficient of *fault friction*, respectively. The use of effective frictional and shear-fracture strength of faults and fault-bounded medium is to incorporate the possible effect of pore-fluid pressure in strength reduction in porous ice-shell materials, with  $\bar{\mu}_\phi = (1 - \lambda_\phi) \mu_\phi$  and  $\bar{\mu}_f = (1 - \lambda_f) \mu_f$ , where  $\lambda_\phi$  and  $\lambda_f$  are the pore fluid ratios in the fault-bounded ice domains and along the fault planes, respectively, and  $\mu_\phi$  and  $\mu_f$  are the coefficient of internal friction and coefficient of friction for the fault-bounded domains and along the fault surfaces, respectively.

We assume that the vertically averaged magnitude of the regional shear stress  $\sigma_s^r$  is equal to the vertically averaged shear strength of the stronger but still deforming region bounding the strike-slip domain with shear strength linearly proportional to a depth of  $H$

(Fig. 5). Under this assumption, the regional-stress magnitude equals to the strength of the bounding region, which can be obtained by

$$\bar{\sigma}_s^r = \bar{Y}^{BR} = \frac{1}{H} \int_0^H (C_{BR} + \bar{\mu}_\phi^{BR} \rho_1 g y) dy = C_{BR} + \frac{1}{2} \bar{\mu}_\phi^{BR} \alpha \rho_1 g h \quad (7)$$

where  $\bar{Y}^{BR}$  is the yield strength of the stronger bounding region,  $C_{BR}$  is the cohesive strength of the bounding-region ice shell,  $\bar{\mu}_\phi^{BR}$  is the effective coefficient of internal friction of the bounding-region ice shell,  $H$  is scaled by  $\alpha = H/h > 1$  as a measure of the regional-stress magnitude relative the stress on the fault plane. By setting  $C_0 = C_{BR}$  and  $\bar{\mu}_\phi^{BR} = \bar{\mu}_\phi$ , assuming that the TSF cut through the entire brittle ice shell, and inserting  $\bar{\sigma}_s^c$ ,  $\bar{Y}$ , and  $\bar{\sigma}_s^r$  defined in Eqs. (5)–(7) into Eq. (2), we can relate fault spacing  $S$  to the brittle ice-shell thickness  $h$  by the following relationship

$$S = \sqrt{\frac{[C_0 - C_1 + \frac{1}{2} \rho_1 g h (\bar{\mu}_\phi - \bar{\mu}_f)]^2 h^2}{\left\{ [C_0 - C_1 + \frac{1}{2} \rho_1 g h (\bar{\mu}_\phi \alpha - \bar{\mu}_f)]^2 - [C_0 - C_1 + \frac{1}{2} \rho_1 g h (\bar{\mu}_\phi - \bar{\mu}_f)]^2 \right\}}} \quad (8)$$

The above solution is valid only if the fault depth are much shallower than the thickness of the brittle ice shell, so the fault can be treated as a half crack in a half elastic space (Pollard and Segall, 1997). As the TSF must cut throughout the entire SPT ice shell (Porco et al., 2006, 2014), the assumption that the TSF are embedded in an elastic half space in Eq. (8) is unrealistic for Enceladus. An additional issue with the solution shown in (8) is that it assumes the creation of strike-slip faults to have been driven by the fault-parallel shear stress *at the surface* only. As indicated in Eq. (2), the fault-parallel shear stress increases with depth and thus the lowest-magnitude shear stress at the surface is unlikely to be the main driving force for the creation of parallel strike-slip faults. In the sections below, we outline two alternative models to address this issue.

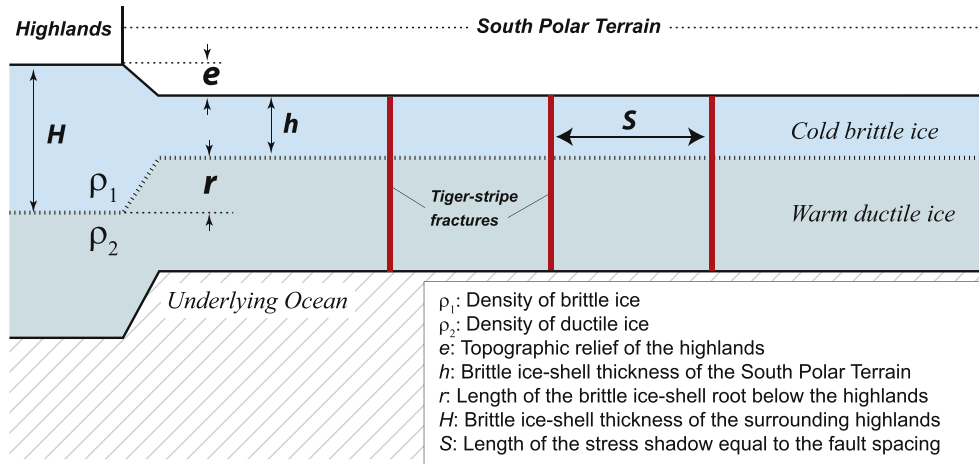


Fig. 5. Model parameters used in calculating the ice-shell thickness in the South Polar Terrain based on the spacing of the tiger-stripe fractures.

#### 4. A stress-rise function model in a perfectly plastic medium

We assume that the medium to be faulted in the SPT ice shell is a perfect plastic material and its shear failure is governed by the Coulomb fracture criterion (also known as the Coulomb failure criterion). Under this assumption, we seek a stress distribution in this medium that satisfies the following boundary conditions:

$$\sigma_{xz}(x=0) = \sigma_s^c \quad (9a)$$

$$\sigma_{xz}(x=\infty) = \sigma_s^r \quad (9b)$$

where  $\sigma_{xz}(x)$  is the shear stress parallel to the strike-slip motion that varies as a function of distance from the fault plane,  $\sigma_s^c$  is shear stress on the fault surface that is equal to the depth-averaged frictional strength on the fault plane, and  $\sigma_s^r$  is a constant and represents the regional/remote shear stress parallel to strike-slip motion. The above equations simply state that the fault-parallel shear stress equals to the fault frictional strength at the fault surface and this shear stress approaches the regional stress at the infinite. Inspired by the solution for stress distribution induced by shear along a mode-III crack (e.g., Pollard and Segall, 1987), we obtain a general solution for the shear-stress distribution induced by motion on a strike-slip fault that cut through an entire brittle crust (Fig. 6A) as shown below:

$$\sigma_{xz}(x) = \sigma_s^r + (\sigma_s^c - \sigma_s^r) \left[ \frac{|x|^{n/m}}{(|x|^n + h^n)^{1/m}} - 1 \right] \quad (10)$$

where  $\sigma_{xz}(x)$  is the depth-independent shear stress,  $x$  is a horizontal axis and its value measures the distance from the fault toward the regional stress,  $\sigma_s^r$  is the regional shear stress,  $\sigma_s^c$  is the shear stress on the fault plane,  $h$  is the depth of the fault that cuts through the entire brittle ice shell,  $n > 0$ , and  $m > 0$  (Fig. 6A). Note that when  $m=2$  and  $n=2$ , the above solution is identical to that shown in Eq. (3), which describes the stress field in an elastic medium induced by shear slip on a crack. As shown below, when  $m=n=1$ , the above equation describes the deformation behavior of a plastic material. Although exploring the physical meaning of the full spectra of  $m$  and  $n$  is beyond the scope of this study, we tentatively conclude that the values of  $m$  and  $n$  in Eq. (11) are governed by the rheology of the material. However, we cannot rule out the possibility that boundary conditions may also play a role in determining the values of  $m$  and  $n$ .

The function  $f(x) = \frac{|x|^{n/m}}{(|x|^n + h^n)^{1/m}}$  in Eq. (10), which is referred to as the *stress-rise function* in this study, dictates how fast the stress

increases from a low value on the fault plane toward the higher regional stress  $\sigma_s^r$  in the infinity. This function has the following properties:

$$f(x=0) = 0 \quad (11a)$$

$$f(x=\infty) = 1 \quad (11b)$$

$$f(x=h) = \frac{1}{2^{1/m}} \quad (11c)$$

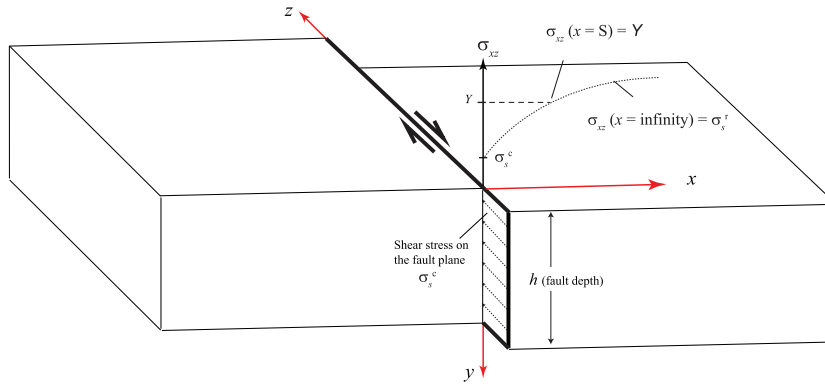
The forms of the stress-rise function for various  $m$  and  $n$  values are shown in Fig. 7. Note that when  $m=1$  and  $n=1$ , the stress-rise function displays the “smoothest” curve, with a gradual decrease in its slope as a function of  $x$  (Fig. 7). Using Eq. (10), we can define the length of the stress shadow,  $S$ , which equals to the fault spacing, from the following expression:

$$\sigma_{xz}(x=S) = Y = \sigma_s^r + (\sigma_s^c - \sigma_s^r) \left[ \frac{S^{n/m}}{(S^n + h^n)^{1/m}} - 1 \right] \quad (12)$$

where  $Y$  is the shear-fracture strength of the fault-bounded medium.

When applying Eq. (12) for modeling TSF spacing in the SPT in particular and parallel strike-slip faults in general, we face the problem of selecting  $m$  and  $n$ . The values of  $n$  and  $m$  in Eq. (12) may be determined by additional rheological constraints or boundary conditions as mentioned above. Rather than appealing for a theoretical determination, we take an empirical approach by noting that extensional joint spacing and the thickness of joint-hosting layer are linearly related (see summary by Bai and Pollard, 2000). In order to test if such a linear relationship also holds for strike-slip faults, we performed a series of sandbox experiments using dry sand and dry crushed walnut shells under strike-slip shear deformation (Lin et al., 2015). First, we used a self-built sliding device to derive the Coulomb fracture strength of the dry sand and crushed walnut shells to be  $\sigma_s = 0.4647\sigma_n + 10.636$  (Pa) and  $\sigma_s = 0.54617\sigma_n + 4.608$  (Pa), respectively, where  $\sigma_s$  and  $\sigma_n$  are shear and normal stresses (see Table 1). Using these two materials, we use an improved paired-shear-zone device of Yin and Taylor (2011) set up in the Department of Earth, Planetary, and Space Sciences at University of California, Los Angeles, to create Riedel shear fractures in two parallel strike-slip shear zones with opposite senses of shear. The experiments lead to the following  $S$ - $h$  relationships:  $S/h = 0.52 \pm 0.1$  for dry sand and  $S/h = 0.84 \pm 0.2$  for crushed walnut shells. Details of the experimental procedures, data acquisition, data analyses, and dynamic scaling of the experimental

(A) Model set-up for the stress-rise-function model with boundary conditions defined at the fault and infinity.



(B) Model set-up for the elastic model with boundary conditions defined at the fault and at the edge of the fault-bounded domain with a characteristic length of L.

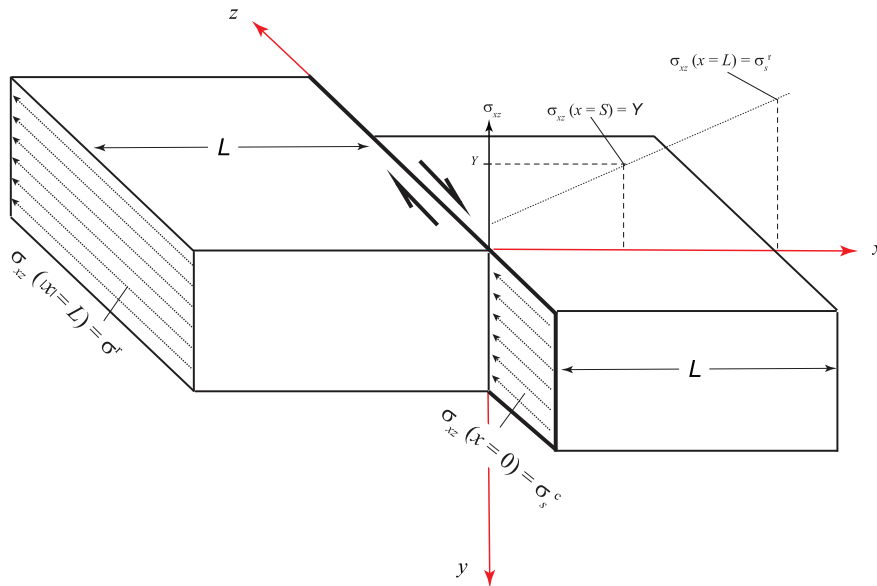


**Fig. 6.** (A) A vertically uniform shear stress is assumed to drive the formation and continuous motion of parallel strike-slip fault in a plastic medium. The off-fault shear stress  $\sigma_{xz}$  satisfies the boundary conditions of  $\sigma_{xz}(x=0) = \sigma_s^c$  and  $\sigma_{xz}(x=\infty) = \sigma_s^r$ . (B) A vertically uniform shear stress is assumed to drive the formation and continuous motion of parallel strike-slip fault in an elastic medium. The off-fault shear stress  $\sigma_{xz}$  satisfies the boundary conditions of  $\sigma_{xz}(x=0) = \sigma_s^c$  and  $\sigma_{xz}(x=L) = \sigma_s^r$ .

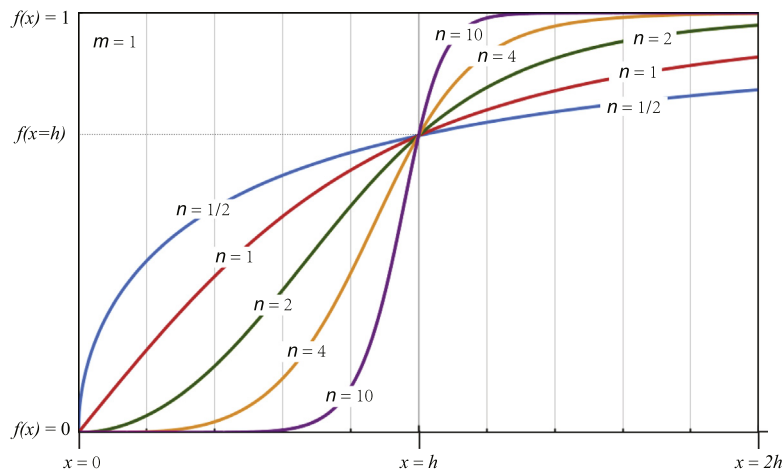


**Fig. 7.** Dependence of stress-rise function on  $m$  and  $n$ . See text for details.

models to crustal/ice-shell-scale deformation on Earth and icy satellites will be presented elsewhere.

The linear functional form for the  $S$ – $h$  relationship requires  $m = n = 1$  in Eq. (12), which in turn leads to the following simple relationship:

$$S = \frac{(Y - \sigma^c)}{(\sigma_s^r - Y)} h \quad (13)$$

Eq. (13) may be used to estimate the brittle ice-shell thickness ( $h$ ) from fault spacing. For example, assuming  $Y = 0.95\sigma_s^r$  and  $\sigma^c = 0.7Y$ , we obtain a relationship of  $S = 5.7h$ . For the 35-km TSF spacing, this relationship requires the brittle ice-shell thickness to be  $\sim 6$  km. The above approach, widely used for modeling joint spacing against joint-hosting layer thickness, involves arbitrary assignments of the relative magnitudes among the shear strength of the fracture-hosting medium, the fault strength, and the regional-stress magnitude (Pollard and Segall, 1987).

In order to avoid these ambiguities in applying Eq. (13), we replace  $\sigma^c$ ,  $Y$ , and  $\sigma_s^r$  in this equation by their vertically averaged values of  $\bar{\sigma}^c$ ,  $\bar{Y}$ , and  $\bar{\sigma}_s^r$  defined in Eqs. (5)–(7). For simplicity, we set  $C_0 = C_2$ ,  $\bar{\mu}_\phi^{BR} = \bar{\mu}_\phi$  (i.e., the mechanical properties of the crustal domain hosting strike-slip faults is the same as those of the stronger and thicker bounding crust). Note that  $H$  in Eq. (7) in the current situation denotes the brittle-crust thickness of the stronger and thicker region bounding the strike-slip-fault crustal domain. Under the above assumptions we obtain a new relationship between  $S$  and  $h$  as:

$$S = \frac{(C_0 - C_1) + \frac{1}{2}\rho_1 gh(\bar{\mu}_\phi - \bar{\mu}_f)}{\frac{1}{2}\rho gh\bar{\mu}_\phi(\alpha - 1)} h \quad (14)$$

The only unknown variable in Eq. (14) is  $\alpha = H/h$ , where  $H = e + h + r$ , with  $e$  as the elevation difference between the SPT and its surrounding regions,  $h$  the thickness of the SPT ice shell, and  $r$  the ice-shell root below the highlands surrounding the SPT (Fig. 5). The other parameters in Eq. (14) can be determined by the mechanical properties of the faults and the fault-bounded domains listed in Table 1. To determine the magnitude of  $\alpha$ , we use the topographic relationship between the SPT and its surrounding highlands. Assuming that (a) a lighter brittle ice shell is compensated by a denser ductile ice shell under Airy isostasy (i.e., the effective elastic thickness of the ice shell is assumed to be zero), and (b) the elevation difference of the SPT and its surrounding region is  $e$  (Fig. 5), the value of  $\alpha$  can be determined by

$$\alpha = \frac{H}{h} = \left(1 + \frac{e}{h} \frac{\rho_2}{\rho_2 - \rho_1}\right) \quad (15)$$

where  $\rho_1$  is the density of the colder and lighter brittle ice, and  $\rho_2$  is the density of the warmer and denser ductile ice. Inserting (15) into (14) leads to

$$S = \frac{2h(C_0 - C_1) + (\bar{\mu}_\phi - \bar{\mu}_f)\rho_1 gh^2}{\bar{\mu}_\phi \rho_1 g e \frac{\rho_2}{(\rho_2 - \rho_1)}} \quad (16)$$

The modified relationship between  $S$  and  $h$  in Eq. (16) is linear only if  $(\bar{\mu}_\phi - \bar{\mu}_f) = 0$ , which is generally the case for both rock and ice (Schulson, 2001, 2002; Schulson and Fortt, 2012; Jaeger et al., 2009). That is,

$$S = \frac{2(C_0 - C_1)}{\bar{\mu}_\phi \rho_1 g e \frac{\rho_2}{(\rho_2 - \rho_1)}} h \quad (17)$$

As shown in Fig. 8, the  $S$ – $h$  relationship is nearly linear when constrained by realistic physical and mechanical parameters for the brittle and ductile ice with  $\bar{\mu}_\phi \neq \bar{\mu}_f$ , consistent with our empirical assumption on the linear  $S$ – $h$  relationship.

The average elevation difference between the SPT and its surrounding highlands (Fig. 1) is  $\sim 0.5$  km (Thomas et al., 2007; Schenk and McKinnon, 2009). The highland region is cut in several places by extensional fractures that radiate from the marginal zones of the SPT. However, there are no active strike-slip structures parallel to the tiger-stripe fractures (Porco et al., 2006; Spencer et al., 2009; Yin and Pappalardo, 2015). This observation implies that the shear-fracture strength of the highland regions may not be critically stressed, and thus, its mechanical strength places an upper limit on the magnitude of regional shear stress that drives the motion on the TSF. This bound on the regional-stress magnitude is now expressed by the elevation difference,  $e$ . For an elevation difference of 500 m (Schenk and McKinnon, 2009), the brittle thickness of the ice shell as required by the 35-km TSF spacing is  $\sim 10.5$  km, assuming that  $\bar{\mu}_\phi = \mu_\phi = 0.58$ ,  $\bar{\mu}_f = \mu_f = 0.4$ ,  $\rho_1 = 940$  kg/m<sup>3</sup>,  $\rho_2 = 990$  kg/m<sup>3</sup>,  $g = 0.133$  m/s<sup>2</sup>, and  $C_0 = 1$  MPa (Fig. 8A) (Table 1).

The coefficient of friction for an ice-on-ice frictional surface varies from 0.37 to 0.53 under Enceladus's condition (Schulson and Fortt, 2012) (Table 1). This range of values requires the thickness of the brittle ice shell in the SPT to be 10.5–11.5 km (Fig. 8B), assuming  $\bar{\mu}_\phi = \mu_\phi = 0.58$ ,  $\rho_1 = 940$  kg/m<sup>3</sup>,  $\rho_2 = 990$  kg/m<sup>3</sup>,  $g = 0.133$  m/s<sup>2</sup>,  $C_0 = 1$  MPa, and  $e = 500$  m. This result indicates that the estimates of the brittle ice-shell thickness are not sensitive to the frictional strength of the TSF, consistent with our derivation of the linear relationship between  $S$  and  $h$  in Eq. (17) when  $\bar{\mu}_\phi = \bar{\mu}_f$ .

Laboratory studies indicate that the cohesive strength for freshwater and salt-water ice at  $-10$  °C and  $-40$  °C is between 1.7 MPa and 5.7 MPa (Table 1), and the uncertainties of the experimental results are typically in the range of  $\pm 0.4$ – $0.6$  MPa (Schulson, 2001). When using the cohesive strength of 0.5–1.5 MPa, the lowest values obtained from the experimental work, we obtain an upper-bound estimate of the brittle ice-shell thickness in the SPT based on the relationship defined in Eq. (17). As shown in Fig. 8C, the low values of the cohesive strength require the brittle ice-shell thickness in the range of 8–18 km, assuming that  $\bar{\mu}_\phi = \mu_\phi = 0.58$ ,  $\bar{\mu}_f = \mu_f = 0.4$ ,  $\rho_1 = 940$  kg/m<sup>3</sup>,  $\rho_2 = 990$  kg/m<sup>3</sup>,  $g = 0.133$  m/s<sup>2</sup>, and  $e = 500$  m.

In contrast to the laboratory-determined cohesive strength on the order of a few MPa, field tests of large floating sea ice indicate that the cohesive strength may be much smaller as a result of its dependence to sample size (Dempsey et al., 1999). For a sea-ice sheet of 1 km in the longest dimension, its tensile strength is estimated to be 11–38 kPa (Dempsey, 2000). Fig. 8D shows how the lower cohesive-strength values impact the estimated thickness of the brittle ice shell in the SPT using the observed 35-km spacing of the tiger-stripe fractures. Specifically, for  $C_0 = 40$  kPa, 30 kPa, and 1 kPa, respectively, the corresponding brittle ice-shell thickness varies from 19.5 to 32 km (Fig. 8D). The plot in Fig. 8D assumes  $\bar{\mu}_\phi = \mu_\phi = 0.58$ ,  $\bar{\mu}_f = \mu_f = 0.4$ ,  $\rho_1 = 940$  kg/m<sup>3</sup>,  $\rho_2 = 990$  kg/m<sup>3</sup>,  $g = 0.133$  m/s<sup>2</sup>, and  $e = 500$  m.

Another uncertainty in estimating the brittle ice-shell thickness comes from the potentially large range of values for the density of the brittle-ice shell. This is because the process for the formation of the SPT ice shell itself is not well understood. For example, if the underlying ocean below the SPT ice shell consists of volatiles and the SPT ice shell has been thickening due to cooling from below (e.g., Manga and Wang, 2007) the ice shell may include pore space filled with gas bubbles. This process would have created a sea-ice-like brittle ice shell with a density lower than that of pure ice. Sea ice on Earth has typical density values between 720 kg/m<sup>3</sup> and 940 kg/m<sup>3</sup> (Timco and Frederking, 1996).

Estimating the density of the SPT ice shell also depends on whether it is composed of crystalline or amorphous ice. Based on a systematic spectral analysis, Newman et al. (2008) argue that

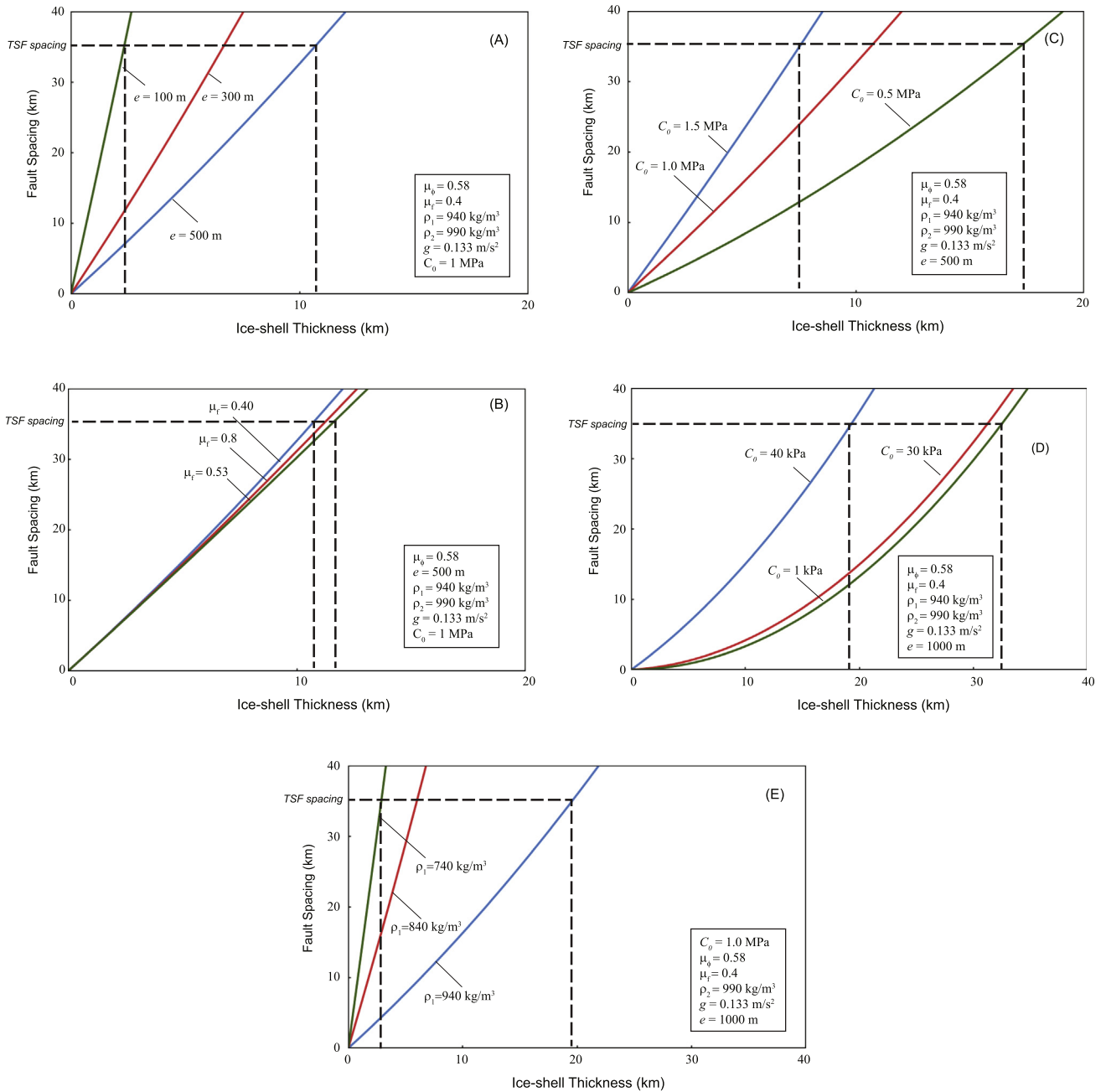


**Fig. 8.** Results of the stress-rise-function model when the strength and stresses used in the model are ice-shell thickness dependent. See text for details. The effect of model parameters on the relationship between the fault spacing and the ice-shell thickness is illustrated in (A) for elevation difference, (B) for frictional strength of the tiger-stripe fractures, (C) and (D) for cohesive strength of the ice shell, and (E) for the density of the brittle ice shell. The colored lines in each graph are defined by the labeled physical quantities. (For interpretation of the references to color in this figure legend, the reader is referred to the web version of this article.)

the surface material near the TSF consists dominantly of crystalline ice, whereas the regions away from the fractures are composed mostly of amorphous ice. The density of amorphous ice at low temperature typically has a density of  $\sim 940 \text{ kg/m}^3$  (e.g., Loerting et al., 2011).

We estimate the density of the ductile ice shell below the SPT based on the work of less et al. (2014). These authors infer from gravity data that the brittle ice shell in the SPT is underlain by a layer that is 8% denser. For a brittle-ice-shell density of  $915 \text{ kg/m}^3$ , the corresponding density of the ductile layer would be  $\sim 990 \text{ kg/m}^3$ . Fig. 8E shows how the choice of density for the brittle-ice shell affects the estimated ice-shell thickness. For a low ice-shell density of  $740 \text{ kg/m}^3$ , the estimated ice-shell thickness is only  $\sim 1.2 \text{ km}$ , whereas for a high ice-shell density of

$940 \text{ kg/m}^3$  the estimated ice-shell thickness is  $\sim 10.5 \text{ km}$ , assuming  $\bar{\mu}_\phi = \mu_\phi = 0.58$ ,  $\bar{\mu}_f = \mu_f = 0.4$ ,  $\rho_2 = 990 \text{ kg/m}^3$ ,  $g = 0.133 \text{ m/s}^2$ ,  $C_0 = 1 \text{ MPa}$ , and  $e = 500 \text{ m}$ .

### 5. An elastic-plate model

In the previous analysis, we assume that the SPT ice shell is a perfect plastic material with its failure strength governed by the Coulomb fracture criterion. We also assume the distribution of the fault-parallel shear stress is governed by a stress-rise function that satisfies the local and remote boundary conditions. In the above approach we neglect the deformation path that leads to the brittle failure driven by the regional stress. That is, the deformation of the perfectly plastic material prior to its local shear

failure could behave elastically, viscously, or visco-elastically, among other possibilities. As a result, the estimated fault depth corresponds to the thickness of the brittle ice shell, which is cut from the top to the bottom of the ice shell by the modeled strike-slip faults. Another important assumption of the stress-rise-function model is that we set the remote stress boundary condition arbitrarily at the infinity.

In order to estimate the elastic ice-shell thickness of the SPT, we assume that the topmost part of the ice shell deforms elastically when the shear stress is below the elastic limit, which is lower than the shear-fracture strength of the ice shell. We also equate the shear stress on the fault plane equals to the fault frictional strength. That is,

$$\sigma_{xz}(x=0, y, z) = \sigma_s^c \quad (18)$$

where  $\sigma_s^c$  is the vertically averaged shear stress acting on the fault plane that is invariant on the fault plane (i.e., in the  $y$  and  $z$  directions).

For the remote stress, we assume that there is a characteristic distance  $L$ , at which the fault-parallel shear stress is equal to the regional stress (Fig. 6B). That is,

$$\sigma_{xz}(|x|=L, y, z) = \sigma_s^r \quad (19)$$

where  $\sigma_s^r$  is the vertically averaged shear stress at a distance of  $L$  from the fault. The vertical normal stress is assumed to lithostatic; its depth-averaged value can be obtained as  $\sigma_{yy} = -\frac{1}{2}\rho_1 gh$ , where  $\rho_1$  is the density of the elastic ice shell. The shear stresses acting on the top and bottom of the elastic plate in the  $x$  and  $z$  directions are set zero; that is,  $\sigma_{yx} = \sigma_{yz} = 0$ . Finally, we assume that the horizontal stress components are invariant with depth, which is expressed by the relationship of  $\frac{\partial\sigma_{xx}}{\partial y} = \frac{\partial\sigma_{zz}}{\partial y} = \frac{\partial\sigma_{xz}}{\partial y} = \frac{\partial\sigma_{zx}}{\partial y} = 0$ .

A general elastic solution of the problem can be obtained by solving a bi-harmonic equation in the  $x$ - $z$  plane (e.g., Fung, 1965; Yin, 1989)

$$\nabla^4 \Phi(x, z) \quad (20)$$

where  $\Phi$  is the Airy stress function. The following form of an Airy stress function satisfied the bi-harmonic equation in (20)

$$\Phi = k_1 xz + \frac{1}{2} k_3 x^2 z + k_7 z^2 \quad (21)$$

where  $k_1$ ,  $k_3$ , and  $k_7$  are constants to be determined by the boundary conditions. This general solution can be related to the horizontal shear- and normal-stress components by (Fung, 1965):

$$\sigma_{xx}(x, z) = \frac{\partial^2 \Phi}{\partial x^2} = k_7 \quad (22a)$$

$$\sigma_{zz}(x, z) = \frac{\partial^2 \Phi}{\partial z^2} = k_3 z \quad (22b)$$

$$\sigma_{xz}(x, z) = \sigma_{zx}(x, z) = -\frac{\partial^2 \Phi}{\partial x \partial z} = -k_1 - k_3 x \quad (22c)$$

The boundary condition  $\sigma_{xz}(x=0, z) = \sigma_s^c$  requires  $k_1 = -\sigma_s^c$ , and the boundary condition  $\sigma_{xz}(x=L, z) = \sigma_s^r$  requires  $k_3 = \left(\frac{\sigma_s^r - \sigma_s^c}{L}\right)$ . We assume that  $k_7$  equals to the vertically averaged lithostatic pressure, and  $\sigma_{xx}(x, z) = \sigma_{yy}(x, z) = -\frac{1}{2}\rho_1 gh$ . Now we have the following solution for the distribution of three stress components parallel and perpendicular to the fault plane:

$$\sigma_{xx}(x, z) = -\frac{1}{2}\rho_1 gh \quad (23a)$$

$$\sigma_{zz}(x, z) = \left(\frac{\sigma_s^r - \sigma_s^c}{L}\right)x \quad (23b)$$

$$\sigma_{xz}(x, z) = \sigma_s^c + \left(\frac{\sigma_s^r - \sigma_s^c}{L}\right)x \quad (23c)$$

Using this solution, we define the critical stress-shadow distance  $S$  by letting  $\sigma_{xz}(x=S, z) = \bar{Y}$ , where  $\bar{Y}$  is the vertically averaged shear-fracture strength. This condition leads to the following relationship:

$$\sigma_{xz}(x=S, z) = \bar{Y} = \sigma_s^c + \left(\frac{\sigma_s^r - \sigma_s^c}{L}\right)S \quad (24)$$

Assuming that the vertically averaged shear-fracture strength of the highlands surrounding the SPT is  $\bar{Y}^{BR} = C_{BR} + \frac{1}{2}\mu_\phi^{BR}\rho_1 g(h + e\frac{\rho_2}{\rho_2 - \rho_1})$ , and replacing  $\sigma_s^r$  and  $\sigma_s^c$  by their vertically averaged values, we obtain

$$S = \frac{L(\bar{Y} - \sigma_s^c)}{(\bar{Y}^r - \sigma_s^r)} = \frac{C_0 + \frac{1}{2}(\mu_\phi - \mu_f)\rho_1 gh L}{C_0 + \frac{1}{2}\mu_\phi \rho_1 g\left(h + e\frac{\rho_2}{\rho_2 - \rho_1}\right) - \frac{1}{2}\mu_f \rho_1 gh} \quad (25)$$

In the above equation we assume that the cohesive strength and coefficient of internal friction of the ice shell within and outside the SPT are the same (i.e.,  $C_{BR} = C_0$ , and  $\mu_\phi^{BR} = \mu_\phi$ ) (see Table 1 for their definitions). Note that the value of  $\bar{Y}^{BR} = C_{BR} + \frac{1}{2}\mu_\phi^{BR}\rho_1 g(h + e\frac{\rho_2}{\rho_2 - \rho_1})$  is obtained under the assumption of Airy isostasy, which means that our estimated elastic thickness of the SPT ice shell should represent an upper bound. This is because the elastic support in converting the topographic relief to the elastic thickness of the surrounding highlands is neglected.

We set the characteristic length scale,  $L$ , to be a half width of the SPT ( $\sim 350$  km) (Fig. 1) in the direction perpendicular to the TSF. The relationship between  $S$  and  $h$  with varying  $C_0$  is shown in Fig. 9A. Note that the mean spacing of 35 km for the TSF in the SPT requires that the cohesive strength must be lower than 30 kPa and the elastic ice-shell thickness is less than 3.5 km assuming that  $\mu_\phi = 0.58$ ,  $\mu_f = 0.4$ ,  $\rho_1 = 940$  kg/m<sup>3</sup>,  $\rho_2 = 990$  kg/m<sup>3</sup>,  $g = 0.133$  m/s<sup>2</sup>, and  $e = 500$  m. For  $C_0 = 0$ ,  $\mu_f$  varies from 0.4 to 0.5 on the TSF, the predicted elastic thickness by this model is <9 km (Fig. 9B).

## 6. Discussion

In this study we examine two stress-shadow models that may explain the formation of the evenly spaced TSF in the SPT of Enceladus. The first model, referred to in this study as the *stress-rise-function model*, is based on a general solution for plastic deformation that contains a characteristic stress-rise function of  $f(x) = \frac{|x|^n}{(|x|^n + h^n)^m}$ , with  $m = n = 1$ . Although the stress-rise-function model does not assign a specific stress-strain relationship for ice-shell deformation prior to its brittle failure, its solutions are geologically and mechanically plausible for two reasons. First, the predicted shear stress satisfies the required boundary conditions at the modeled fault plane and at the far field. Second, the solutions derived from this model yield a linear (for constant ice-shell and fault strength) or nearly linear (for depth-dependent ice-shell and fault strength) relationship between fault spacing and the ice-shell thickness. The assumed linear  $S$ - $h$  relationship is consistent with the linear relationship between joint spacing and the thickness of joint-hosting layers under brittle deformation (Bai and Pollard, 2000) and our own preliminary sandbox experiments (Lin et al., 2015). Hence, we interpret our estimated ice-shell thickness based on the stress-rise-function model to represent the brittle-layer thickness of the SPT ice shell.

Our second model, referred to in this study as the *elastic-plate model*, is based on a solution for stress distribution in an infinitely long elastic plate that has a characteristic length scale for defining the width of the plate (Fig. 6B). As the TSF have finite length, the solutions obtained from this model may approximate the stress state along a straight line perpendicular to the mid-point of the modeled faults. Thus, the inferred spacing and the estimated

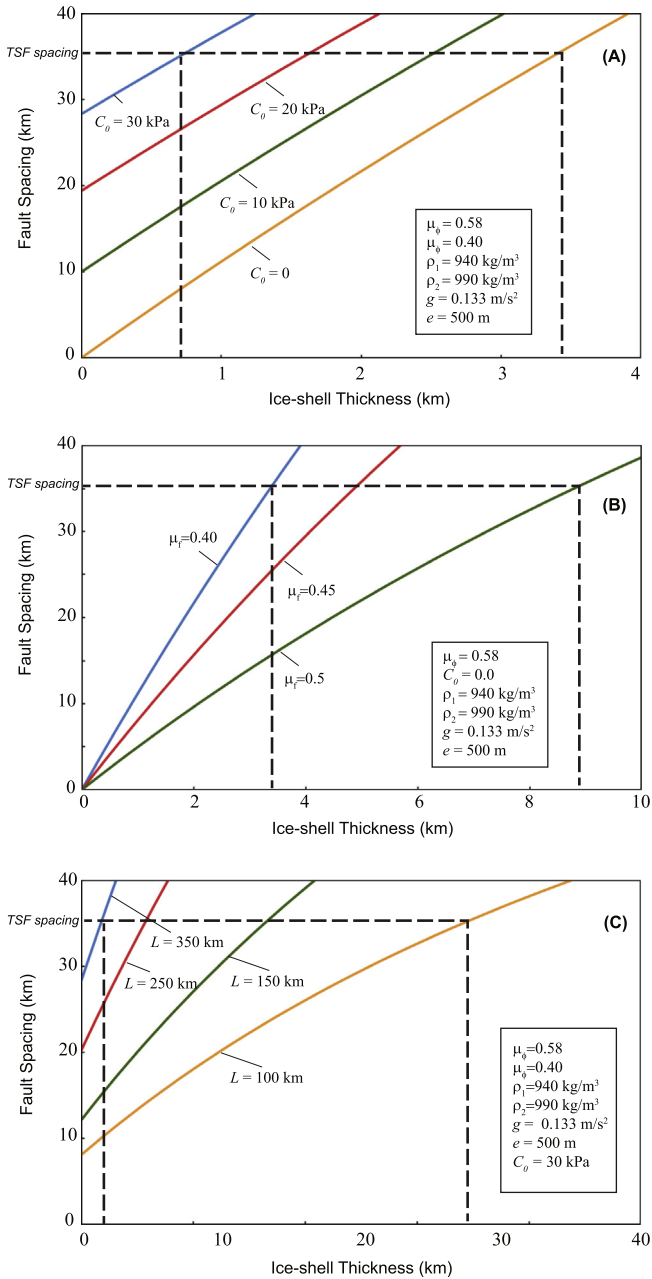


**Fig. 9.** Results of the elastic-plate model. The effect of model parameters on the relationship between the fault spacing and the ice-shell thickness is illustrated in (A) for the cohesive strength of the ice shell, (B) for the frictional strength of the tiger-stripe fractures, and (C) for the characteristic length scale that defines the stress gradient. See text for details.

elastic thickness are valid if the left-slip TSF were first initiated in the center and then propagated laterally toward the two ends. Another important assumption in this model is that the shear stress rises linearly with a gradient of  $\left(\frac{\sigma_s^i - \sigma_s^c}{L}\right)$ , where  $\sigma_s^i$  represents the regional stress,  $\sigma_s^c$  represents the stress on the fault surface, and  $L$  represents a half width of the SPT in the direction perpendicular to the TSF (Fig. 6B). It is possible that the size of the SPT started small and has expanded in aerial extent through time. If this were the case, the value of  $L$  has to increase with time. Fig. 9C illustrates the effect of variable  $L$  values on fracture spacing; a smaller  $L$  value requires a thicker elastic ice shell whereas a larger  $L$  value requires a thinner elastic ice shell. This relationship can also be alternatively stated: for the same ice shell thickness, the larger the  $L$  value, the

wider the fault spacing. One way to think of the qualitative physical meaning of this latter statement is that a larger  $L$  value requires a lower stress gradient, and it takes a longer distance (i.e., wider fault spacing) for the stress value to reach the yield strength of the ice shell.

Combining the stress-rise-function and elastic-plate models, the observed spacing of the TSF in the SPT (Fig. 1) requires that (a) the brittle ice-shell thickness to be  $\sim 30$  km (Fig. 8D), (b) the elastic ice-shell thickness to be  $\sim 0.7$  km (Fig. 9A), and (c) the cohesive strength of the SPT ice shell to be  $\sim 30$  kPa (Fig. 9). As mentioned above, the estimated brittle and elastic ice-shell thickness is an upper bound because the assumed regional stress could be smaller than the vertically averaged shear strength of the highland regions surrounding the SPT. In this scenario, the predicted low cohesive strength of  $\sim 30$  kPa implies that the magnitude of the tensile stress in the SPT terrain is too low to be able to create penetrating tensile cracks that cut through the entire brittle layer of the SPT ice shell (Lee et al., 2005; Rudolph and Manga, 2009). However, one should keep in mind that if the two models are decoupled and a high cohesive strength of 1 MPa is used for the brittle ice shell, the predicted brittle layer thickness would be about 11 km (Fig. 8C).

We note that our predicted thickness of the SPT ice shell is remarkably consistent with other independent estimates. Analyzing Enceladus’s degree 2 gravity determined by Cassini by considering its rapid (1.37 day) synchronous spin, McKinnon (2015) suggests that the compensation depth (shell thickness) of Enceladus’ global (degree 2) ice shell is  $\sim 50$  km and the compensation depth (shell thickness) beneath the SPT is 30–40 km (cf., Iess et al., 2014). The latter is consistent with our estimated brittle ice-shell thickness of  $\sim 30$  km. Iess et al. (2014) show that the observed gravity-to-topography ratios of Enceladus are consistent with an elastic thickness of  $< 0.5$  km. Similar estimates of elastic-shell thickness are also made by flexural analysis (Giese et al., 2008) and relaxation studies (Bland et al., 2012) of crater morphology. This is consistent with our estimate of  $\sim 0.7$  km for the SPT elastic ice-shell thickness.

The models proposed in this work may be tested in two ways. First, the predicted relationship between fault spacing and layer thickness may be examined by analogue sandbox experiments. Second, a more sophisticated numerical model with a more realistic rheology involving viscous creeping of the warm ice, which may host the root zones of the TSF, is needed to better model the three-dimensional variation of stress state in the SPT. This is because the initiation of a new fracture cutting across the SPT ice has to overcome both the brittle and ductile strength of the whole ice shell. Finally, the porosity of the ice shell should be considered in future modeling, as its distribution may lead to a large spatial variation in mechanical strength and density distribution of the ice shell (e.g., Lee et al., 2005), which were not considered in our simple model.

### 7. Conclusions

We present the first mechanical analysis on the formation of evenly spaced strike-slip faults using realistic boundary conditions and rheology for the ice shell of Enceladus. Two quantitative models based on the stress-shadow concept for explaining extensional joint spacing are proposed in this study for explaining the formation of the evenly spaced tiger-stripe fractures in the South Polar Terrain of Enceladus: (1) an empirically based stress-rise-function model that simulates the brittle-deformation process during the formation of evenly spaced strike-slip faults, and (2) a plate model that relates fault spacing to the elastic thickness of the plate. When applying the models for the initiation and development of the tiger-stripe fractures (TSF) in the South Polar Terrain

(SPT) of Enceladus, the mutually consistent solutions of the two models, as constrained by the mean spacing of the TSF at  $\sim 35$  km, requires the brittle ice-shell thickness to be  $\sim 30$  km, the elastic thickness to be  $\sim 0.7$  km, and the cohesive strength of the ice shell to be  $\sim 30$  kPa for the South Polar Terrain that hosts the tiger-stripe fractures. The consistency between the brittle and elastic thicknesses of the SPT ice shell determined in this study and those estimated by other independent methods supports the plausibility of our proposed stress-shadow mechanism for the formation of the tiger-stripe fractures on Enceladus.

## Acknowledgments

An extremely thorough review and very constructive comments by Stephanie Johnston have greatly improved the scientific content and clarity of the original manuscript. This work also benefits greatly from several stimulating discussions and more importantly encouragement from Dr. Carolyn Porco throughout the project. She careful reading and comments led to further clarification of the concepts and interpretations presented in this study. AY's work on the mechanics of strike-slip fault is supported by a grant from the Tectonics Program, US National Science Foundation. Work by RTP was carried out at the Jet Propulsion Laboratory, California Institute of Technology, under a contract with the National Aeronautics and Space Administration.

## References

- Bai, T., Pollard, D.D., 2000. Fracture spacing in layered rocks: A new explanation based on the stress transition. *J. Struct. Geol.* 22 (1), 43–57.
- Bland, M.T. et al., 2012. Enceladus' extreme heat flux as revealed by its relaxed craters. *Geophys. Res. Lett.* 39 (17). <http://dx.doi.org/10.1029/2012GL052736>, L17204.
- Collins, G.C., Goodman, J.C., 2007. Enceladus' south polar sea. *Icarus* 189 (1), 72–82.
- Dempsey, J.P., 2000. Research trends in ice mechanics. *Int. J. Solids Struct.* 37 (1), 131–153.
- Dempsey, J.P., Adamson, R.M., Mulmule, S.V., 1999. Scale effects on the in-situ tensile strength and fracture of ice. Part II: First-year sea ice at resolute, NWT. *Int. J. Fract.* 95 (1–4), 347–366.
- Fung, Y.C., 1965. *Foundations of Solid Mechanics*, vol. 351. Prentice-Hall, Englewood Cliffs, NJ, pp. 463–470.
- Giese, B. et al., 2008. Enceladus: An estimate of heat flux and lithospheric thickness from flexurally supported topography. *Geophys. Res. Lett.* 35 (24).
- Gioia, G. et al., 2007. Unified model of tectonics and heat transport in a frigid Enceladus. *Proc. Natl. Acad. Sci. USA* 104 (34), 13578–13581.
- Helfenstein, P. et al., 2006. Patterns of fracture and tectonic convergence near the South Pole of Enceladus. *Lunar Planet. Sci.* 37, Abstract no. 2182.
- Helfenstein, P. et al., 2008. Enceladus south polar terrain geology: New details from Cassini ISS high resolution imaging. *American Geophysical Union (Fall), Abstract*.
- Hutter, K., 1983. *Theoretical Glaciology: Material Science of Ice and the Mechanics of Glaciers and Ice Sheets*, vol. 1. Springer.
- Iess, L. et al., 2014. The gravity field and interior structure of Enceladus. *Science* 344 (6179), 78–80.
- Jaeger, J.C., Cook, N.G.W., Zimmerman, R., 2009. *Fundamentals of rock mechanics*. John Wiley & Sons.
- Lachenbruch, A.H., 1961. Depth and spacing of tension cracks. *J. Geophys. Res.* 66 (12), 4273–4292.
- Lee, S., Pappalardo, R.T., Makris, N.C., 2005. Mechanics of tidally driven fractures in Europa's ice shell. *Icarus* 177 (2), 367–379.
- Lin, J.C., Zuza, A.V., Yin, A., 2015. Quantifying the relationship between strike-slip fault spacing and brittle crust thickness in continental settings based on sandbox experiments. *AGU Annual Meeting (Fall)*, San Francisco (abstract).
- Loerting, T. et al., 2011. How many amorphous ices are there? *Phys. Chem. Chem. Phys.* 13 (19), 8783–8794.
- Manga, M., Wang, C.Y., 2007. Pressurized oceans and the eruption of liquid water on Europa and Enceladus. *Geophys. Res. Lett.* 34 (7).
- Matsuyama, I., Nimmo, F., 2008. Tectonic patterns on reoriented and despun planetary bodies. *Icarus* 195, 459–473.
- McKinnon, W.B., 2015. Effect of Enceladus's rapid synchronous spin on interpretation of Cassini gravity. *Geophys. Res. Lett.* 42. <http://dx.doi.org/10.1002/2015GL063384>.
- Mellor, M., Cole, D.M., 1983. Stress/strain/time relations for ice under uniaxial compression. *Cold Reg. Sci. Technol.* 6 (3), 207–230.
- Newman, S.F. et al., 2008. Photometric and spectral analysis of the distribution of crystalline and amorphous ices on Enceladus as seen by Cassini. *Icarus* 193 (2), 397–406.
- Nur, A., 1982. The origin of tensile fracture lineaments. *J. Struct. Geol.* 4 (1), 31–40.
- Olgin, J.G., Smith-Konter, B.R., Pappalardo, R.T., 2011. Limits of Enceladus's ice shell thickness from tidally driven tiger stripe shear failure. *Geophys. Res. Lett.* 38 (2), 10.1029/2010GL044950.
- Patthoff, D.A., Kattenhorn, S.A., 2011. A fracture history on Enceladus provides evidence for a global ocean. *Geophys. Res. Lett.* 38, L18201.
- Pollard, D.D., Segall, P., 1987. Theoretical displacements and stresses near fractures in rock: With applications to faults, joints, veins, dikes, and solution surfaces. In: Atkinson, B.K. (Ed.), *Fracture Mechanics of Rocks*, pp. 277–349.
- Porco, C.C. et al., 2006. Cassini observes the active south pole of Enceladus. *Science* 311, 1393–1401.
- Porco, C., DiNino, D., Nimmo, F., 2014. How the geysers, tidal stresses, and thermal emission across the South Polar Terrain of Enceladus are related. *Astron. J.* 148, Article no. 45.
- Roberts, J.H., Nimmo, F., 2008. Tidal heating and the long-term stability of a subsurface ocean on Enceladus. *Icarus* 194 (2), 675–689.
- Roy, M., Royden, L.H., 2000a. Crustal rheology and faulting at strike-slip plate boundaries: 1. An analytic model. *J. Geophys. Res.: Solid Earth (1978–2012)* 105 (B3), 5583–5597.
- Roy, M., Royden, L.H., 2000b. Crustal rheology and faulting at strike-slip plate boundaries: 2. Effects of lower crustal flow. *J. Geophys. Res.: Solid Earth (1978–2012)* 105 (B3), 5599–5613.
- Rudolph, M.L., Manga, M., 2009. Fracture penetration in planetary ice shells. *Icarus* 199 (2), 536–541.
- Schenk, P.M., McKinnon, W.B., 2009. One-hundred-km-scale basins on Enceladus: Evidence for an active ice shell. *Geophys. Res. Lett.* 36, L16202.
- Schulson, E.M., 2001. Brittle failure of ice. *Eng. Fract. Mech.* 68, 1839–1887.
- Schulson, E.M., 2002. Compressive shear faults in ice: Plastic vs. Coulombic faults. *Acta Mater.* 50 (13), 3415–3424.
- Schulson, E.M., Fortt, A.L., 2012. Friction of ice on ice. *J. Geophys. Res.: Solid Earth (1978–2012)* 117 (B12).
- Sinha, N.K., 1978. Rheology of columnar-grained ice. *Exp. Mech.* 18 (12), 464–470.
- Smith-Konter, B., Pappalardo, R.T., 2008. Tidally driven stress accumulation and shear failure of Enceladus's tiger stripes. *Icarus* 198, 435–451.
- Spencer, J.R. et al., 2009. Enceladus: An active cryovolcanic satellite. In: Dougherty, M., Esposito, L., Krimigis, S. (Eds.), *Saturn from Cassini-Huygens*. Springer, Netherlands, pp. 683–724.
- Taylor, M.H., Yin, A., 2009. Active faulting on the Tibetan Plateau and sounding regions relationships to earthquakes, contemporary strain, and late Cenozoic volcanism. *Geosphere* 5 (3), 199–214.
- Taylor, M. et al., 2003. Conjugate strike-slip faulting along the Bangong-Nujiang suture zone accommodates coeval east–west extension and north–south shortening in the interior of the Tibetan Plateau. *Tectonics* 22 (4), 1043. <http://dx.doi.org/10.1029/2002TC001383>.
- Thomas, P.C. et al., 2007. Shapes of the saturnian icy satellites and their significance. *Icarus* 190 (2), 573–584.
- Thomas, P.C. et al., 2015. Enceladus's measured physical libration requires a global subsurface ocean. *Icarus* 264, 37–47.
- Timco, G.W., Frederking, R.M.W., 1996. A review of sea ice density. *Cold Reg. Sci. Technol.* 24 (1), 1–6.
- Walker, C.C., Bassis, J.N., Liemohn, M.W., 2012. On the application of simple rift basin models to the south polar region of Enceladus. *J. Geophys. Res.: Planets (1991–2012)* 117 (E7).
- Yin, A., 1989. Origin of regional, rooted low-angle normal faults: A mechanical model and its tectonic implications. *Tectonics* 8 (3), 469–482.
- Yin, A., 2010. Cenozoic tectonic evolution of Asia: A preliminary synthesis. *Tectonophysics* 488 (1), 293–325.
- Yin, A., Harrison, T.M., 2000. Geologic evolution of the Himalayan-Tibetan orogen. *Annu. Rev. Earth Planet. Sci.* 28 (1), 211–280.
- Yin, A., Pappalardo, R.T., 2015. Gravitational spreading, bookshelf faulting, and tectonic evolution of the South Polar Terrain of Saturn's moon Enceladus. *Icarus* 260, 409–439.
- Yin, A., Taylor, M.H., 2011. Mechanics of V-shaped conjugate strike-slip faults and the corresponding continuum mode of continental deformation. *Geol. Soc. Am. Bull.* 123 (9–10), 1798–1821.
- Yin, A. et al., 2015. A possible seismic gap and high earthquake hazard in the North China Basin. *Geology* 43 (1), 19–22.